Event Classification in Heterostructured Scintillators With Limited Readout Information Using Neural Networks

Carsten Lowis, *Graduate Student Member, IEEE*, Fiammetta Pagano, Marco Pizzichemi, Karl-Josef Langen, Karl Ziemons, *Member, IEEE*, and Etiennette Auffray, *Member, IEEE*

***Abstract*—To improve coincidence time resolution (CTR) in time-of-flight positron emission tomography (TOF-PET), various approaches have been explored, including the use of novel materials like heterostructured scintillators. These scintillators combine different materials with complementary properties like Bismuth Germanate for its high detection efficiency and EJ232 for fast timing. By layering these materials on a micrometer scale, energy sharing between them becomes possible, enabling fast timing, while maintaining high detection efficiency. For TOF-PET applications, scalable electronics are essential. While earlier models characterized heterostructured scintillators in analog, single-pixel setups, the digital and scalable systems required for full positron emission tomography (PET) scanners present additional challenges due to increased signal complexity. In this study, we explored neural networks to characterize heterostructured scintillators using parameters available in scalable systems. We trained one neural network to identify photoelectric events and another one to estimate the amount of energy sharing between the two materials. The method demonstrated promising results using multiple combinations of the aforementioned parameters, with prediction accuracy for photoelectric events ranging from 91.6% to 96.8%, and a mean average error in the energy sharing estimation between 7.7 and 43.9 keV. This suggests the potential application of heterostructured scintillators in scalable readout electronics for full TOF-PET systems.**

***Index Terms*—Energy sharing, heterostructures, machine learning scintillators, signal processing, time-of-flight positron emission tomography (TOF-PET).**

Received 16 December 2024; accepted 3 February 2025. Date of publication 10 February 2025; date of current version 4 July 2025. This work was supported in part by the CERN Budget for Knowledge Transfer to Medical Applications, and in part by the Wolfgang Gentner Programme of the German Federal Ministry of Education and Research under Grant 13E18CHA. *(Corresponding author: Carsten Lowis.)*

This work did not involve human subjects or animals in its research.

Carsten Lowis is with EP, CERN, 1211 Geneva, Switzerland, and also with the Faculty of Medicine, RWTH Aachen University, 52056 Aachen, Germany (e-mail: carsten.lowis@cern.ch).

Fiammetta Pagano is with EP, CERN, 1211 Geneva, Switzerland, also with the Department of Physics, University Milano-Bicocca, 20126 Milan, Italy, and also with the Institute of Instrumentation for Molecular Imaging, 46022 Valencia, Spain.

Marco Pizzichemi is with EP, CERN, 1211 Geneva, Switzerland, and also with the Department of Physics, University Milano-Bicocca, 20126 Milan, Italy.

Karl-Josef Langen is with the Faculty of Medicine, RWTH Aachen University, 52056 Aachen, Germany.

Karl Ziemons is with the Faculty of Biomedical Engineering and Technomathematics, FH-Aachen University of Applied Sciences, 52428 Jülich, Germany.

Etiennette Auffray is with EP, CERN, 1211 Geneva, Switzerland.

Digital Object Identifier 10.1109/TRPMS.2025.3540559

I. Introduction

A MORE accurate time-of-flight (TOF) resolution is one of the driving forces increasing the performance of positron emission tomography (PET). This medical imaging technique allows for the assessment of metabolic processes in patients useful for diagnostic and treatment related purposes using radioactive β^{+}-tracers. The annihilation of positrons and electrons create two coincident photons with an energy of 511 keV, which are emitted with an angle of around 180° from each other. By detecting both photons, their origin can be pinned to the line between the two corresponding detectors, called the line of response (LoR). In time-of-flight PET (TOF-PET), timing information is used to determine the position of the annihilation point on the LoR. The advantages of this technique have been discussed to great extent already in the past [1], [2], [3], [4]. They include better rejection of random coincident events and an improvement in signal-to-noise ratio (SNR). Because SNR is inversely proportional to the coincidence time resolution (CTR). This results in a better image quality with the same acquisition time or less dose and a shorter measurement time without a loss of SNR. Modern scanners like the PET-CT scanner Biograph Vision from Siemens are capable of reaching 214-ps CTR [5].

An optimization of the CTR requires improvements in the whole detection chain from readout electronics, over the photodetectors to the scintillation materials used [5], [6], [7], [8], [9], [10]. One challenging aspect about scintillation materials is the tradeoff between fast time resolution and other properties like the detection efficiency of the incident gamma rays [11].

To work around this problem, the use of heterostructured scintillators has already given very promising results in past studies [9], [12], [13], [14], [15]. Here, two materials with complementary properties are combined in order to benefit globally from their individual beneficial characteristics. In our case, one material is BGO (high stopping power but slow scintillation kinetics) and the other is Eljen technology EJ232 (fast scintillation kinetics but low stopping power [14]). This combination has already proven to be suitable to further study the energy sharing mechanism, since they are optically compatible and have a very similar light yield [12], [13]. The incident gamma rays is most likely being absorbed in the scintillator with a high stopping power, but then the recoil electrons (70 μm of projected range for 511-keV electrons in

BGO [12]) can deposit their energy in both materials. This leads to an improvement in the timing properties depending on how much energy is deposited in the fast scintillator, since the scintillation kinetics of the heterostructure is given by the linear combination of the scintillation kinetics of the two components, weighted by the energy deposited in each case [13]. One of the challenges is that in order to fully characterize the scintillation events, it is necessary to know not only the total energy deposited in the scintillator, but also the energy deposited in each material. This is essential as the timing characteristics will vary from event to event due to these differences.

In previous studies [12], [13], this event classification has been done by acquiring the maximum amplitude and the integrated charge of the silicon photomultiplier signal and selecting events in an analytical approach.

Currently available scalable readout electronics used for TOF-PET do not allow for the simultaneous measurement of the maximum amplitude and the integrated charge [6], [17], making the aforementioned classification method not feasible. In order to solve this issue and also to make this classification automatic we want to investigate a neural network based classification method which is adaptable to a combination of different readout parameters. Since the classification is based on the amount of energy deposited in each of the two materials, we require a minimum of two readout parameters. The use of machine learning to optimize the signal processing for TOF-PET has been shown to be a successful approach [18], [19].

The use of neural networks has already been established for event classification in phoswich detectors [20], [21]. Similar to heterostructure scintillators, phoswich detectors also use multiple different scintillation materials. Pulse shape discrimination is required to distinguish which material has emitted the scintillation light. A key difference is that in phoswich detectors, this discrimination is typically more distinct, whereas in heterostructured scintillators, energy sharing between the materials produces a mixed signal. This work aims to extend our understanding of the use of neural networks for pulse shape discrimination in heterostructure scintillators.

II. Methods

A. Measurement Setup

The heterostructured scintillator was coupled to a Broadcom NUV-MT SiPM (AFBR-S4N44P014M, Broadcom NUV-MT [22]) biased with an overvoltage of 15 V (47-V bias voltage) set up against a reference detector consisting of an LSO:Ce:0.4Ca ($2\times2\times3$ mm^3) scintillator coupled to the same SiPM model and also biassed with 15-V overvoltage. Cargille Meltmount (refractive index $n = 1.58$) was used as an optical coupling material between SiPM and the scintillators. A positron emitting ^{22}Na-source was placed in between the two scintillators in order to measure coincident events of 511 keV gamma rays originating from the positron–electron annihilation. The SiPMs are read out by a custom amplifier that splits the signal in two in order to independently analyze the energy using an analog amplifier and the time using an high-frequency amplifier. The signals are finally digitized by a LeCroy DDA735Zi oscilloscope (3.5-GHz bandwidth, 20-Gs/s sample rate) [5]. More details for the setup can be found in [5]. We measured a heterostructure of $3\times3\times15$ mm^3 and alternating layers with a size of 200 μm for EJ232 and 100 μm for BGO. There was no coupling material used between the alternating layers. The measurement setup can be seen in Fig. 1.

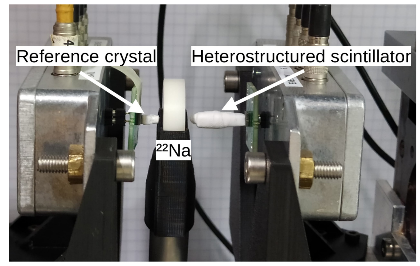

Fig. 1. Measurement setup for coincident events with reference crystal (left), heterostructured scintillator (right), and a ^{22}Na positron source (center).

B. Signal Waveform Analysis

As the first step, we extracted the amplitude and integrated charge from the signal waveforms of the energy signal of the heterostructured scintillator. This was done by using build-in functions of the oscilloscope. No post processing was applied to the signal waveforms. These were used to distinguish photoelectric events and the ratio of energy deposition in each materials. This classification concept is shown in Fig. 2 and was discussed to great length in prior studies [13]. Photoelectric events are defined by their total energy deposition being between 440 and 665 keV. An additional parameter to extract the energy information and that can be found in other readout systems [5], [15] is the time over threshold (TOT). We set the thresholds to 10 and 20 mV. 10 mV was the lowest threshold that allowed for a stable readout without noise and 20 mV was the highest threshold that would not cut out any photoelectric events. A sketch with the three extracted parameters is also illustrated in Fig. 3.

C. Machine-Learning-Based Event Classification

1) Classification of Photoelectric Events: Our first aim was to identify photoelectric events using a dense neural network. The ground-truth labels were set to 1 (photoelectric event) or 0 (compton scattered event) based on the classification described in Section II-B. As dataset the parameter combinations used were the max amplitude together with the TOT at 10 mV (AMP_TOT), the integrated charge together with the same TOT (INT_TOT) and two TOTs at 10 and 20 mV (TOT_TOT).

As preprocessing, each parameter was normalized to be between 0 and 1. This allowed for the training of more general and reliable models since the scale of each parameter is kept consistent. The total number of events acquired was 479 102. This dataset was split into two parts with 70% for training (335 372 events) and 30% (143 730 events) for the final evaluation.

For the network architecture, we have chosen a dense neural network with an input layer of two values, a variable amount of

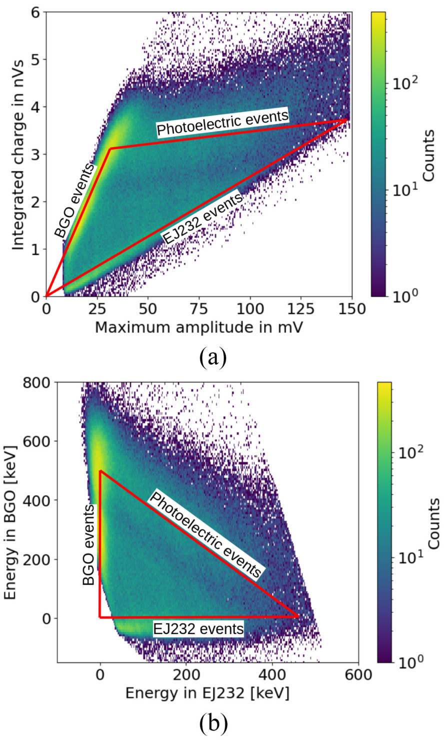

Fig. 2. (a) 2-D histogram of the integrated charge against the maximum amplitude of the SiPM signal. (b) 2-D histogram of the energy deposited in each material obtained through a coordinate transformation from plot (a). The red lines indicate all photoelectric events (at 511-keV total deposited energy) and events with energy deposited in only one material (BGO events, EJ232 events).

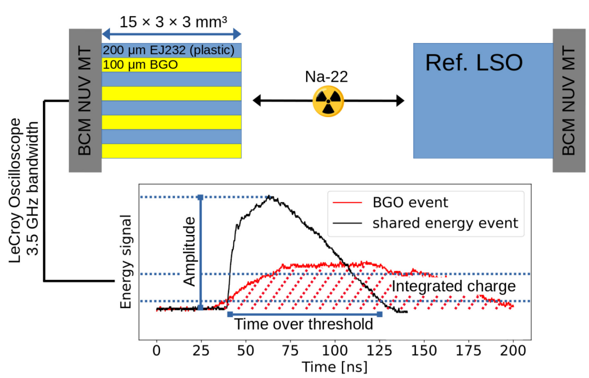

Fig. 3. Schematic measurement setup (top) together with an exemplary output signal for BGO and shared energy events. The measurement parameters that have been readout in this study are also shown.

hidden layers with a variable amount of nodes, each followed by a rectified linear unit (ReLU) activation functions. The following output layer contained a single value and a sigmoid activation function to ensure a value between 0 and 1. Finally this output was set to 0 or 1 in order to maximize the classification accuracy in the training dataset.

The models were trained for 10 epochs and with variable batch sizes. We used the Adam optimizer with a learning rate of 0.01, binary cross entropy as loss function and accuracy as metric.

To estimate the optimal hyperparameters, the training was performed in fivefold cross validation with a grid search using different combinations of the number of hidden layers (ranging from 1 to 32), number of nodes per hidden layer (ranging from 2 to 64) and different batch sizes (ranging from 100 to 2000). The final architecture was chosen individually for all cases based on the highest classification accuracy.

TABLE I
OPTIMAL HYPERPARAMETERS DEPENDENT ON DIFFERENT INPUTS FOR THE PROPOSED DENSE NEURAL NETWORK TO IDENTIFY PHOTOELECTRIC EVENTS

Hyperparameter	AMP_TOT	INT_TOT	TOT_TOT
Number of hidden layers	2	8	4
Number of nodes per hidden layer	16	16	16
Batch size	500	500	1000

The model performance was evaluated using the accuracy, sensitivity and specificity. This evaluation was repeated using the isolated test dataset. We also looked at how much the misclassified photoelectric events differed in energy from the upper (665 keV) and lower (440 keV) energy limits used in the ground-truth classification.

2) Estimation of Energy Sharing Ratio: In the next step we aimed at estimating the ratio of shared energy between BGO and EJ232 in photoelectric events using a second dense neural network. As dataset, we used the three parameter combinations mentioned before (AMP_TOT, INT_TOT, and TOT_TOT) in a 70/30 train/test split, but excluding non photoelectric events. This resulted in a dataset of 194 714 events total (136 300 events for training and 58 414 for testing). Then, as ground-truth label, we took the ratio between the energy deposited in EJ232 and the total amount of deposited energy.

For the network architecture we chose the same before, only modifying the output layer by using a ReLU activation function instead of a sigmoid activation function.

The training procedure was also only slightly modified from the aforementioned one by using mean-squared error as loss function as evaluation metric since we want to estimate a ratio and not a binary classification. The optimal hyperparameters (number of hidden layers, number of nodes per hidden layer and batch size) were again chosen by fivefold cross validation with a grid search using different combinations resulting in individually optimized network architectures.

The model performance was evaluated using the mean average error and validated using the isolated test dataset.

III. RESULTS

A. Classification of Photoelectric Events

Table I shows the hyperparameters that were taken for each model used to classify photoelectric events. These combinations showed the optimal accuracy during training. Further increasing the complexity by adding more hidden layers or nodes per hidden layer only changed the performance slightly within the error range. Reducing the complexity resulted in unstable performance results, since the training did not converge every time.

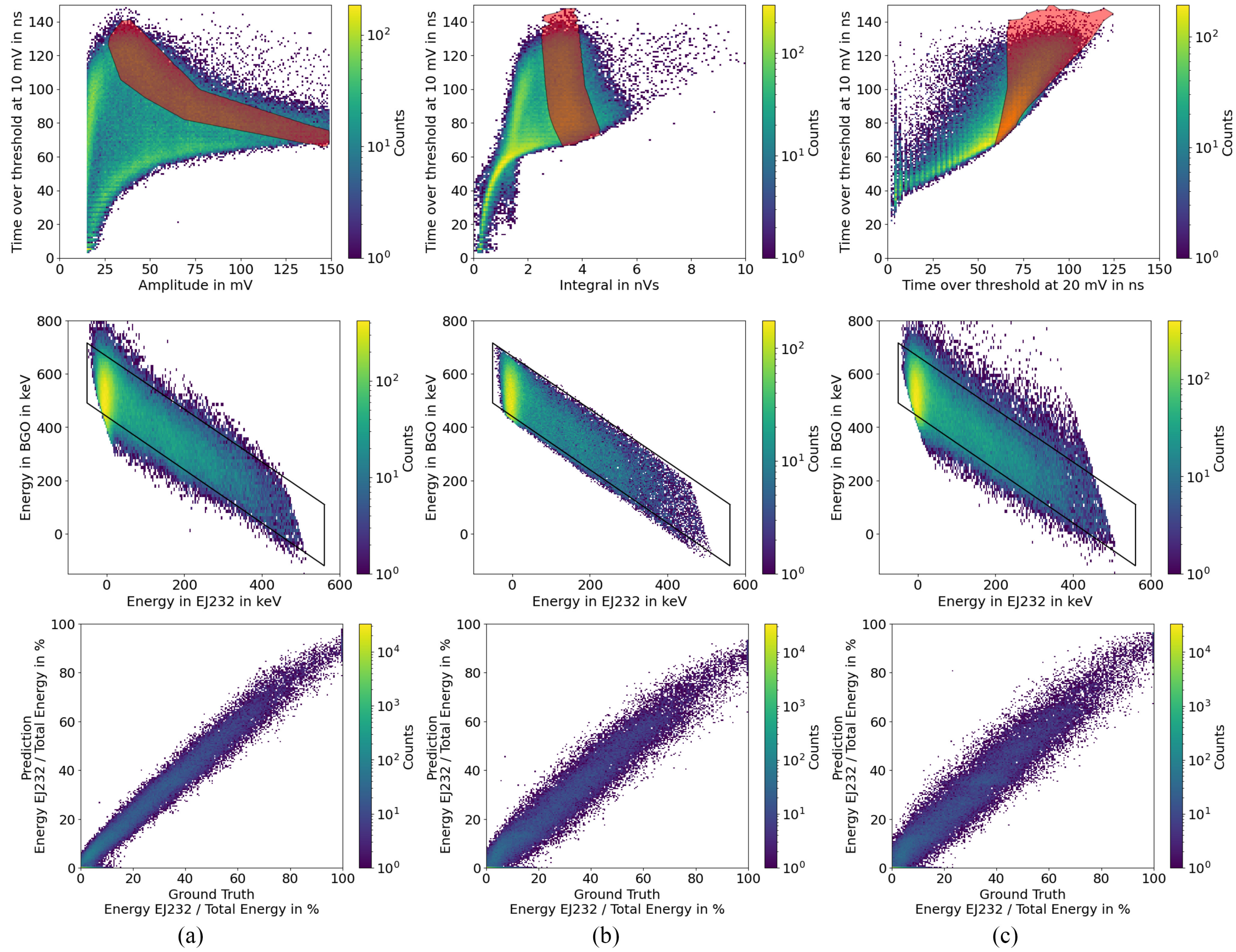

Fig. 4. Exemplary visualization of the neural network-based classification [(a) AMP_TOT maximum amplitude and TOT at 10 mV, (b) INT_TOT integrated charge and TOT at 10 mV, and (c) TOT_TOT time over threshold at 10 mV and time over threshold at 20 mV]. On the top are 2-D histograms of the readout parameter against each other with a red box highlighting the region of predicted photoelectric events. The center plots show 2-D histograms of the predicted photoelectric events together with their actual energy deposited. The black box indicates the area which corresponded to photoelectric events in the ground-truth classification. The plots on the bottom show 2-D histogram of predicted against ground-truth ratio of energy deposited in EJ232 for photoelectric events.

The resulting model performances can be seen in Table II. The best classification accuracy was achieved with the parameter combination INT_TOT at 96.8% and a mean energy error for false positive events of 7.7 keV using the test dataset. The parameter combinations AMP_TOT and TOT_TOT showed a very similar performance.

B. Estimation of Energy Sharing Ratio

The network hyperparameter which resulted in the lowest mean average error when predicting the ratio of shared energy in EJ232 are shown in Table III for each parameter combination. Similar to the previous training, it was observed, that a increasing the architecture complexity further did not lead to an improvement outside of the error range, while decreasing the complexity lead to an unreliable convergence.

The detailed optimal model performances can be seen in Table IV. The lowest mean average error was achieved with the parameter combination AMP_TOT at 1.89%, while for the parameter combinations INT_TOT and TOT_TOT a similar result was reached.

TABLE II
PERFORMANCE COMPARISON OF THE NEURAL NETWORK TO IDENTIFY PHOTOELECTRIC EVENTS USING DIFFERENT INPUT PARAMETERS, EVALUATED BY FIVEFOLD CROSS-VALIDATION AND ISOLATED TEST DATASET

Input combination	**AMP_TOT**	**INT_TOT**	**TOT_TOT**
Train dataset; 5-fold cross validation			
Accuracy in %	91.5 ± 1.2	98.0 ± 0.5	92.0 ± 0.1
Sensitivity in %	87.0 ± 2.3	97.4 ± 1.0	87.0 ± 0.4
Specificity in %	95.0 ± 0.9	98.5 ± 0.4	96.0 ± 0.4
Test dataset			
Accuracy in %	92.6	96.8	91.6
Sensitivity in %	94.6	98.5	91.0
Specificity in %	91.2	95.6	92.0
mean energy error for false positive events in keV	36.2	7.7	43.9

IV. DISCUSSION

A. Classification of Photoelectric Events

The event classification of photoelectric events is illustrated as an example in Fig. 4 for the different readout parameter combinations. On the top, 2-D histograms of how the events are distributed when looking at the different input parameter

TABLE III
OPTIMAL HYPERPARAMETERS DEPENDENT ON DIFFERENT INPUTS FOR THE PROPOSED DENSE NEURAL NETWORK TO ESTIMATE THE RATIO OF SHARED ENERGY IN EJ232 IN PHOTOELECTRIC EVENTS

Hyperparameter	AMP_TOT	INT_TOT	TOT_TOT
Number of hidden layers	2	2	4
Number of nodes per hidden layer	32	16	16
Batch size	1000	500	500

TABLE IV
PERFORMANCE COMPARISON OF THE NEURAL NETWORK TO ESTIMATE THE RATIO OF SHARED ENERGY IN EJ232 PHOTOELECTRIC EVENTS USING DIFFERENT INPUT PARAMETERS, EVALUATED BY FIVEFOLD CROSS-VALIDATION AND ISOLATED TEST DATASET

Input combination	AMP_TOT	INT_TOT	TOT_TOT
Train dataset; 5-fold cross validation			
Mean squared error in %	1.87 ± 0.01	2.69 ± 0.03	2.96 ± 0.10
Test dataset			
Mean squared error in %	1.89	2.76	2.87

combinations used for machine learning models are shown. Highlighted in red are the regions that were predicted as photoelectric events. The intrinsic non linearity of the TOT measurements of the deposited energy [23], [24] can clearly be observed as these selected regions take rather complex forms. In the center the distribution of the predicted photoelectric events are visualized when looking at their energy distribution visualized as 2-D histograms. The black box indicates the region between 440 and 665 keV of total energy deposition. In the ground-truth classification, events in this range were rated as photoelectric events. It can clearly be seen that for the parameter combination INT_TOT the predicted events are mostly within the black box, while there is a larger spread outside for the parameter combination AMP_TOT and TOT_TOT. This is expected, since the integrated charge of the SiPM signal alone already gives a better estimation of the total deposited energy compared to the other tested parameters, since the light yield of the two materials is very similar. This is also reflected in the classification accuracy and mean energy error for false positive events in Table II.

B. Estimation of Energy Sharing Ratio

Additionally, we implemented a second neural network that determines the ratio between the energy shared with EJ232 and the total deposited energy in photoelectric events. The bottom part of Fig. 4 shows this distribution in the ground truth and the corresponding prediction in a 2-D histogram for the different readout parameter combinations. It can be seen in all three plots that the ground truth and the predictions correlate well with each other. While the model with AMP_TOT achieves the lowest spread. This is consistent with the comparison of mean average errors from Table IV. This result was to be expected, as the maximum amplitude can be taken as a linear measure for the energy deposition in EJ232 [13].

The estimation of the energy sharing ratio of photoelectric events can be beneficial due to the possibility of using a multi-kernel TOF image reconstruction in a PET system [25], [26].

V. CONCLUSION AND OUTLOOK

In this work we proposed a possible method to identify photoelectric events and the amount of shared energy in heterostructured scintillators with measurement parameters that are available in readout electronics which can be scaled to a full PET system. Whereas the conventional method requires the readout of specifically the integrated charge and the maximum amplitude of the SiPM signal together with a semi-manual coordinate transformation, the presented method is more independent in its input parameters (as shown with three example combinations: AMP_TOT, INT_TOT, and TOT_TOT) and can work automatically.

The measurements to validate the method were performed using a heterostructured scintillator consisting of alternating layers of 100-μm BGO and 200-μm EJ232 with a total size of $3\times3\times15$ mm^3. In a first part, a neural network was trained to identify if event originated from a photoelectric effect or not. We were able to reproduce the ground truth with an accuracy of 91.6%–96.8%. In a second part, we trained another neural network to estimate the ratio of shared energy in photoelectric events. Here, it was possible to reproduce the ground truth with a mean-squared error of 1.89%–2.87% (assuming 511-keV energy deposition in total: 9.7–14.7 keV). It was found that the classification of photoelectric events worked best with the parameter combination INT_TOT. This can be explained by the similar light yield of both materials (BGO and EJ232), which leads to an almost proportional relationship between the detected photons and the integrated charge. On the other hand, the estimation of the fraction of shared energy gave optimal results with the parameter combination AMP_TOT. This can be explained by considering the maximum amplitude as a linear measure of the energy deposited in EJ232. However, both the classification of photoelectric events and the estimation of the energy sharing ratio were possible using only TOT values (TOT_TOT).

This suggests the possible application of heterostructured scintillators to a full system and therefore follow-up studies are foreseen on optimising the ground truth classification, since this was one limiting factor of this study. The method has been tested using TOT, amplitude and integrated charge values obtained by the oscilloscope. In an actual use case these values would be acquired by a dedicated readout circuit resulting in less ideal conditions. Therefore an application of this method with the FastIC readout ASIC is foreseen [6]. With this readout electronic, the simultaneous acquisition of the maximum amplitude and a TOT is possible, which is the equivalent of the AMP_TOT parameter combination investigated in this work.

ACKNOWLEDGMENT

This work has been performed in the framework of the Crystal Clear Collaboration. The authors would like to thank

Dominique Deyrail for his help in the heterostructure preparation.

All authors declare that they have no known conflicts of interest in terms of competing financial interests or personal relationships that could have an influence or are relevant to the work reported in this article.

REFERENCES

[1] W. W. Moses and S. E. Derenzo, "Prospects for time-of-flight PET using LSO scintillator," *IEEE Trans. Nucl. Sci.*, vol. 46, no. 3, pp. 474–478, Jun. 1999, doi: 10.1109/23.775565.

[2] M. Conti, "Focus on time-of-flight PET: The benefits of improved time resolution," *Eur. J. Nucl. Med. Mol. Imag.*, vol. 38, no. 6, pp. 1147–1157, Jun. 2011, doi: 10.1007/s00259-010-1711-y.

[3] C. Lois et al., "An assessment of the impact of incorporating time-of-flight information into clinical PET/CT imaging," *J. Nucl. Med.*, vol. 51, no. 2, pp. 237–245, Feb. 2010, doi: 10.2967/jnumed.109.068098.

[4] J. Van Sluis et al., "Performance characteristics of the digital biograph vision PET/CT system," *J. Nucl. Med.*, vol. 60, no. 7, pp. 1031–1036, Jul. 2019, doi: 10.2967/jnumed.118.215418.

[5] S. Gundacker, R. M. Turtos, E. Auffray, M. Paganoni, and P. Lecoq, "High-frequency SiPM readout advances measured coincidence time resolution limits in TOF-PET," *Phys. Med. Biol.*, vol. 64, no. 5, Feb. 2019, Art. no. 55012, doi: 10.1088/1361-6560/aafd52.

[6] S. Gomez, J. M. Fernández-Tenllado, J. Alozy, M. Campbell, R. Manera, and J. Mauricio, "FastIC: A highly configurable ASIC for fast timing applications," in *Proc. IEEE Nucl. Sci. Symp. Med. Imag. Conf. (NSS/MIC)*, Piscataway, NJ, USA, Oct. 2021, pp. 1–4, doi: 10.1109/NSS/MIC44867.2021.9875546.

[7] N. Kratochwil, E. Auffray, and S. Gundacker, "Exploring Cherenkov emission of BGO for TOF-PET," *IEEE Trans. Radiat. Plasma Med. Sci.*, vol. 5, no. 5, pp. 619–629, Sep. 2021, doi: 10.1109/TRPMS.2020.3030483.

[8] G. Terragni et al., "Time resolution studies of thallium based Cherenkov semiconductors," *Front. Phys.*, vol. 10, Mar. 2022, Art. no. 785627, doi: 10.3389/fphy.2022.785627.

[9] R. M. Turtos, S. Gundacker, E. Auffray, and P. Lecoq, "Towards a metamaterial approach for fast timing in PET: Experimental proof-of-concept," *Phys. Med. Biol.*, vol. 64, no. 18, Sep. 2019, Art. no. 185018, doi: 10.1088/1361-6560/ab18b3.

[10] N. Kratochwil, S. Gundacker, P. Lecoq, and E. Auffray, "Pushing Cherenkov PET with BGO via coincidence time resolution classification and correction," *Phys. Med. Biol.*, vol. 65, no. 11, Jun. 2020, Art. no. 115004, doi: 10.1088/1361-6560/ab87f9.

[11] D. R. Schaart, "Physics and technology of time-of-flight PET detectors," *Phys. Med. Biol.*, vol. 66, no. 9, May 2021, Art. no. 9TR01, doi: 10.1088/1361-6560/abee56.

[12] F. Pagano, N. Kratochwil, M. Salomoni, M. Pizzichemi, M. Paganoni, and E. Auffray, "Advances in heterostructured scintillators: Toward a new generation of detectors for TOF-PET," *Phys. Med. Biol.*, vol. 67, no. 13, Jul. 2022, Art. no. 135010, doi: 10.1088/1361-6560/ac72ee.

[13] F. Pagano, N. Kratochwil, L. Martinazzoli, C. Lowis, M. Paganoni, and M. Pizzichemi, "Modeling scintillation kinetics and coincidence time resolution in heterostructured scintillators," *IEEE Trans. Nucl. Sci.*, vol. 70, no. 12, pp. 2630–2637, Dec. 2023, doi: 10.1109/TNS.2023.3332699.

[14] G. Konstantinou et al., "A proof-of-concept of cross-luminescent metascintillators: Testing results on a BGO:BaF 2 metapixel," *Phys. Med. Biol.*, vol. 68, no. 2, Jan. 2023, Art. no. 25018, doi: 10.1088/1361-6560/acac5f.

[15] F. Pagano et al., "Nanocrystalline lead halide perovskites to boost time-of-flight performance of medical imaging detectors," *Adv. Mater. Int.*, vol. 11, no. 10, Apr. 2024, Art. no. 2300659, doi: 10.1002/admi.202300659.

[16] "ELJEN technology EJ232 datasheet." 2021. [Online]. Available: https://eljentechnology.com/products/

[17] A. D. Francesco et al., "TOFPET$_2$: A high-performance ASIC for time and amplitude measurements of SiPM signals in time-of-flight applications," *J. Inst.*, vol. 11, no. 3, Mar. 2016, Art. no. C03042, doi: 10.1088/1748-0221/11/03/C03042.

[18] F. Loignon-Houle et al., "Improving timing resolution of BGO for TOF-PET: A comparative analysis with and without deep learning," *EJNMMI Phys.*, vol. 12, no. 1, p. 2, Jan. 2025, doi: 10.1186/s40658-024-00711-6.

[19] Y. Onishi, F. Hashimoto, K. Ote, and R. Ota, "Unbiased TOF estimation using leading-edge discriminator and convolutional neural network trained by single-source-position waveforms," *Phys. Med. Biol.*, vol. 67, no. 4, Feb. 2022, Art. no. 4NT01, doi: 10.1088/1361-6560/ac508f.

[20] R. P. Li, H. D. Wang, J.-B. Lu, C. Li, H. Qu, and Z. Situ, "A self-organizing feature map neural network for Compton suppression in phoswich detector," *Nucl. Instrum. Methods Phys. Res. A Acceler. Spectr. Detectors Assoc. Equip.*, vol. 1059, Feb. 2024, Art. no. 168987, doi: 10.1016/j.nima.2023.168987.

[21] R. Panahi, S. A. H. Feghhi, S. R. Moghadam, and S. M. Zamzamian, "Simultaneous alpha and gamma discrimination with a phoswich detector using a rise time method and an artificial neural network method," *Appl. Radiat. Isotopes*, vol. 154, Dec. 2019, Art. no. 108881, doi: 10.1016/j.apradiso.2019.108881.

[22] "Broadcom NUV MT SiPM datasheet." 2023. [Online]. Available: https://www.broadcom.com/products/optical-sensors/silicon-photomultiplier-sipm/high-performance-sipm-nuv-mt/

[23] F. Powolny, E. Auffray, H. Hillemanns, P. Jarron, P. Lecoq, and T. C. Meyer, "A novel time-based readout scheme for a combined PET-CT detector using APDs," *IEEE Trans. Nucl. Sci.*, vol. 55, no. 5, pp. 2465–2474, Oct. 2008, doi: 10.1109/TNS.2008.2004036.

[24] P. F. Manfredi, A. Leona, E. Mandelli, A. Perazzo, and V. Re, "Noise limits in a front-end system based on time-over-threshold signal processing," *Nucl. Instrum. Methods Phys. Res. A Acceler. Spectr. Detectors Assoc. Equip.*, vol. 439, nos. 2–3, pp. 361–367, Jan. 2000, doi: 10.1016/S0168-9002(99)00852-9.

[25] P. Mohr et al., "Image reconstruction analysis for positron emission tomography with heterostructured scintillators," *IEEE Trans. Radiat. Plasma Med. Sci.*, vol. 7, no. 1, pp. 41–51, Jan. 2023, doi: 10.1109/TRPMS.2022.3208615.

[26] N. Efthimiou, N. Kratochwil, S. Gundacker, A. Polesel, M. Salomoni, and E. Auffray, "TOF-PET image reconstruction with multiple timing kernels applied on Cherenkov radiation in BGO," *IEEE Trans. Radiat. Plasma Med. Sci.*, vol. 5, no. 5, pp. 703–711, Sep. 2021, doi: 10.1109/TRPMS.2020.3048642.